

# Propensity rules and interference effects in laser-assisted photoionization of helium and neon

Mattias Bertolino, David Busto, Felipe Zapata, and Jan Marcus Dahlström  
*Department of Physics, Lund University, Box 118, SE-221 00 Lund, Sweden*

(Dated: July 17, 2022)

We investigate the angle-resolved photoelectron spectra from laser-assisted photoionization for helium and neon atoms using an *ab initio* method based on time-dependent surface flux and configuration interaction singles. We find that the shape of the distributions can be interpreted using a propensity rule, an intrinsic difference in the absorption and emission processes, as well as interference effects between multiple paths to the final angular momentum state. In neon we find that the difference between absorption and emission is hidden in the first sideband due to the multiple competing  $m$  channels. Together, this aids the understanding of the formation of minima in the angular distributions, which can be transferred to an improved understanding on photoionization time delays in attosecond science.

## I. INTRODUCTION

Photoionization is a fundamental process in nature where absorption of a photon by an atom leads to the emission of a photoelectron and to the creation of a positive ion:  $A + \gamma \rightarrow A^+ + e^-$ . The photoelectric effect is possible only when the energy of the photon,  $\hbar\omega$ , is sufficiently large to overcome the electron binding energy of the atom,  $I_p$ . Although the process is explained qualitatively as a one-electron transition from an occupied atomic orbital to a continuum of states, the quantitative photoionization rates are affected by electron-electron correlation effects in the atom, as evidenced in works based on many-body perturbation theory [1–3]. Given photons with a wavelength that is larger than the size of the atom,  $a_0 = 5.29 \times 10^{-11}$  m, the electronic transitions can be simplified to follow the dipole *selection rules*, where the angular momentum of the electron must change by one unit:  $\Delta\ell = \pm 1$ . This reduces the complexity of the problem to a finite set of continua that can be reached by the photoelectron. As a complement to the dipole selection rules, Fano proposed a *propensity rule*, which states that absorption of light favours increasing the electron angular momentum,  $\ell \rightarrow \ell + 1$ , over decreasing the angular momentum,  $\ell \rightarrow \ell - 1$  [4]. This simple rule explains why in neon the probability to reach the  $d$ -wave from the initial  $2p$  orbital is larger than the probability to reach the  $s$ -wave. As with most simple rules, there are also some notable exceptions, e.g. in photoionization from  $3p$  orbital in argon in the vicinity of the Cooper minimum, where the  $d$ -wave contribution becomes very small due to a vanishing dipole element for the transition [5].

In recent years, novel light sources have made it possible to study light–matter interactions in more extreme conditions where the atoms are subject to more intense short-wavelength fields [6], multi-color fields [7–9] and short pulses with duration on the femtosecond and attosecond time scale [10]. One class of problems that has attracted attention is *laser-assisted photoionization*, where an atom is photoionized using radiation of short wavelength, typically extreme ultraviolet radiation (XUV), but with an additional long-

wavelength laser field, typically in the infrared range (IR), which *dresses* the atom:  $A + \gamma_{\text{XUV}} \pm q\gamma_{\text{IR}} \rightarrow A^+ + e^-$ . In this case, the electron is ionized by the XUV field and then subsequently interacts with the IR field leading to laser-driven continuum–continuum transitions. Again all transitions follow the dipole selection rules, but the strength of the laser field can be made large to study quasi-classical electron trajectories and quantum interference effects [11, 12]. In the multi-cycle pulse limit, the resulting photoelectron angle-resolved spectrum includes a main peak at an energy given by the XUV photoelectric effect and a number of sideband peaks due to the increasing number of interactions with the IR field:  $E_{\text{kin}} = \hbar\omega_{\text{XUV}} \pm q\hbar\omega_{\text{IR}} - I_p$ . In the case where the IR field is weak, the strength of the sidebands decreases with each order as expected from perturbation theory with a probability determined by the intensity power law in atomic units:  $P_q \propto (I_{\text{IR}})^q$ .

Laser-assisted photoionization has been studied analytically using time-dependent Volkov states, which by their closed-form solution allow for efficient calculations of cross-sections for laser-assisted scattering and ionization [13–15]. More accurate numerical studies have been performed by perturbation theory within the single-active electron (SAE) approximation [16, 17] and by many-body perturbation theory at the level of one-photon Random Phase Approximation with Exchange (RPAE) with uncorrelated continuum–continuum transitions for closed shell atoms [18] and for photodetachment of negative ions [19]. Recently, a gauge-invariant two-photon RPAE approach has been demonstrated [20]. Numerical simulations have also been performed in the time domain within the SAE [21–24], for helium [25] and many-electron atoms, e.g. neon by R-matrix theory [26, 27] and argon by Density Functional Theory (DFT) [28]. Many-electron correlations in nonlinear photoionization has also been studied by time-dependent theories based on Configuration Interaction Singles (CIS) [29] and Multi-Configuration Self-Consistent Fields (MCSCF) [30]. Laser-assisted photoionization is an important process in attosecond science, where it is at the core of both pulse character-

ization techniques using the RABBIT technique [31] and for measurement of atomic delays in photoionization [32, 33]. Recently, atomic delay measurements have been performed with angular resolution [34–36]. This has evidenced that subtle differences in absorption and emission processes in the continuum–continuum transitions can lead to a strong dependency on the atomic delay with angle of emission, incomplete quantum interference in RABBIT measurements and to qualitatively different angular distributions of photoelectrons, as explained by Busto et al. by extending Fano’s propensity rule to continuum–continuum transitions [35].

In this paper, we perform *ab-initio* simulations of laser-assisted photoionization by propagating the Time-Dependent Schrödinger Equation (TDSE) within the Configuration Interaction Singles approximation (TDCIS) [37, 38]. This allows us to examine the angular distributions and propensity rules in laser-assisted photoionization of helium and neon atoms for both the first sideband and higher-order sidebands generated by absorption of multiple IR photons. We find different angular distributions formed by absorption and emission processes in the continuum, and we are able to verify that the propensity rules can be extended to higher-order continuum–continuum transitions driven by the IR field. The paper is structured as follows. In Section II, our method is described along the relevant laser parameters. In Section III, we present our results of the numerical simulations. Finally, in Section V, we draw conclusions of the presented data and discuss potential topics for future studies. Atomic units ( $\hbar = e = m_e = 4\pi\epsilon_0 = 1$ ) are used through out this paper if not specifically stated.

## II. METHOD

In this section we describe our method to compute laser-assisted photoionization from closed-shell atoms. In part A we describe the vector potential used to model the electromagnetic fields, in part B we review the TDCIS ansatz, in part C we present details of our t-SURFF implementation and in part D we give some more details on our numerical implementation.

### A. Field description

The numerical experiments are carried out with Gaussian XUV- and IR-pulses, linearly polarized along the quantization axis  $\hat{z}$ , that are overlapped in time and defined by a vector potential given by

$$A = [A_0^{\text{XUV}} \sin(\omega_{\text{XUV}}t) + A_0^{\text{IR}} \sin(\omega_{\text{IR}}t)] \times \exp\left[-2 \ln(2) \frac{t^2}{\tau^2}\right], \quad (1)$$

where  $A_0^{\text{XUV}} = 0.005$  a.u. and  $A_0^{\text{IR}} = 0.003$  a.u. which yields a peak intensity of the IR pulse of  $5.6 \times 10^9$  W/cm<sup>2</sup>. The duration of the pulses is given by

$\tau = 410$  a.u.  $\approx 10$  fs and the frequency of the IR-field is given by  $\omega_{\text{IR}} \approx 1.55$  eV to match a Ti-Saph. laser system.

### B. TDCIS ansatz

The TDCIS ansatz [37] for the many electron wave function is

$$|\Psi(t)\rangle = \alpha_0(t) |\Phi_0\rangle + \sum_a^{\text{occ}} \sum_p^{\text{exc}} \alpha_a^p(t) |\Phi_a^p\rangle, \quad (2)$$

where  $|\Phi_0\rangle$  is the Hartree-Fock ground state and the singly excited states  $|\Phi_a^p\rangle$  are constructed using the framework of second quantization,

$$|\Phi_a^p\rangle = \frac{1}{\sqrt{2}} \{ \hat{c}_{p+}^\dagger \hat{c}_{a+} + \hat{c}_{p-}^\dagger \hat{c}_{a-} \} |\Phi_0\rangle, \quad (3)$$

where  $\hat{c}_{p\sigma}^\dagger$  creates an electron in the virtual (exc) orbital  $p$  with spin  $\sigma$ ,  $|\phi_{p\sigma}\rangle$ , while  $\hat{c}_{a\sigma}$  creates a hole in the initially occupied (occ) orbital  $a$  with spin  $\sigma$ ,  $|\varphi_{a\sigma}\rangle$ . The ansatz in Eq. (3) assures that the spin *singlet* state character of the closed-shell initial state is maintained also for excited states. Similarly, we adopt the *gerade* formulation of TDCIS to make full use of the symmetry in magnetic quantum numbers,  $m_p = m_a$ , for linearly polarized fields [39]. In TDCIS the time dependence is found only in the complex amplitudes,  $\alpha_0(t)$  and  $\alpha_a^p(t)$ , and the static orbitals are found by solving the mean-field HF problem without fields present. The time evolution of the complex amplitudes is found by projecting the ansatz in Eq. (2) onto the TDSE with a laser-interaction Hamiltonian, as shown in Ref. [38, 39]. Here, we consider light-matter interaction within the dipole approximation given by  $V_I(t) = A_z(t) \hat{p}_z$ , where  $E_z(t) = -\partial A_z(t) / \partial t$  is the electric field with linear polarization along the  $\hat{z}$ -direction. The choice of helium and neon is done on the basis of their different initial angular momentum state and hence their difference in the accessible continuum-state after the absorption of one XUV-photon. In addition, both helium and neon are well-described by the truncated basis of the TDCIS theory.

### C. Implementation of t-SURFF with TDCIS

Within TDCIS theory, the excited many-body state can be expressed as one-electron time-dependent orbitals [37],

$$\chi_a(\mathbf{r}, t) = \sum_p^{\text{exc}} \alpha_a^p(t) \phi_p(\mathbf{r}), \quad (4)$$

associated with each created hole,  $a$ . The time-dependent orbitals can also be expanded as

$$\chi_a(\mathbf{r}, t) = \frac{1}{r} \sum_{\ell_p} \psi_{\ell_p m_a}^a(r, t) Y_{\ell_p m_a}(\hat{r}), \quad (5)$$

where  $\ell_p$  runs over all possible angular momenta attainable by the electron. The t-SURFF method relies on knowledge of the photoelectron wavefunction,  $\chi_a(\mathbf{r}_c, t)$ , at a given radius,  $r_c < r_{\text{ecs}}$ , at all times,  $t$ , and then makes use of the approximate Volkov states to account of field-induced dynamics of the photoelectron beyond  $r_c$  [40]. We use a modified Volkov Hamiltonian,

$$\hat{H}_a^{(V)}(t) = \frac{\hat{p}^2}{2} + A_z(t)\hat{p}_z - \varepsilon_a, \quad (6)$$

where  $\hat{p}^2 = -\nabla^2$  and  $\hat{p}_z = -i\partial/\partial z$ , to model the dynamics of the time-dependent orbital in the region far from the ion, where Coulomb interactions can be neglected. The energy of the photoelectron depends on the binding energy of orbital  $a$  in accordance with Koopman's theorem,  $I_p = -\varepsilon_a$ . The time-dependent orbitals that satisfy the TDSE with the Hamiltonian from Eq. (6) are

$$\chi_{\mathbf{k},a}^{(V)}(\mathbf{r}, t) = \frac{1}{(2\pi)^{3/2}} \exp[i\mathbf{k} \cdot \mathbf{r}] \times \exp \left[ -i \int_{t_{\text{ref}}}^t dt' \left\{ \frac{k^2}{2} + A_z(t')k_z - \varepsilon_a \right\} \right], \quad (7)$$

which are plane waves with a time-dependent phase.

The spectral amplitudes for laser-assisted photoionization are found using a complex amplitude for the overlap of time-dependent orbitals in the outer region,  $r > r_c$ , using a radial Heaviside operator acting at  $r_c$ ,  $\hat{\theta}(r_c)$ , defined as

$$b_{\mathbf{k},a}(t) = \left\langle \chi_{\mathbf{k},a}^{(V)}(t) \left| \hat{\theta}(r_c) \right| \chi_a(t) \right\rangle. \quad (8)$$

The complex amplitude in Eq. (8) becomes the scattering amplitude when the time is evaluated at a late hour,  $t = T$ , after which all external fields have ended and after which the photoelectron wave packet have propagated far away from the ion [40]. We obtain a final expression for the scattering coefficients in t-SURFF given by

$$b_{\mathbf{k},a}(T) = i\sqrt{\frac{2}{\pi}} \int_{-\infty}^T dt \exp \left[ i \int_{t_{\text{ref}}}^t d\tau \left\{ \frac{k^2}{2} + A_z(\tau)k_z - \varepsilon_a \right\} \right] \times \sum_{\ell_p} \left\{ (-i)^{\ell_p} \frac{1}{2} \left( kr_c j'_{\ell_p}(kr_c) + j_{\ell_p}(kr_c) \right) \psi_{\ell_p m_a}^a(r_c, t) Y_{\ell_p m_a}(\Omega_{\mathbf{k}}) - \frac{(-i)^{\ell_p}}{2} r_c j_{\ell_p}(kr_c) \psi_{\ell_p m_a}^{a'}(r_c, t) Y_{\ell_p m_a}(\Omega_{\mathbf{k}}) + \frac{i}{2\sqrt{\pi}} r_c A_z(t) \sqrt{2\ell_p + 1} \psi_{\ell_p m_a}^a(r_c, t) \sum_{\ell=\ell_p \pm 1} (-i)^\ell \frac{j_\ell(kr_c)}{2\ell + 1} C_{\ell_p m_a, 10}^{\ell m_a} C_{\ell_p 0, 10}^{\ell 0} Y_{\ell m_a}(\Omega_{\mathbf{k}}) \right\}, \quad (9)$$

where  $j_\ell(kr)$  is the spherical bessel function of order  $\ell$  and  $j'_\ell(kr)$  is its derivative, both evaluated at  $kr$ . Further  $Y_{\ell,m}(\Omega_{\mathbf{k}})$  is the spherical harmonic of order  $\ell$  and  $m$  evaluated at angle  $\Omega_{\mathbf{k}} \equiv (\theta_{\mathbf{k}}, \varphi_{\mathbf{k}})$  and  $C_{\ell m, 10}^{\ell' m}$  is the Clebsch-Gordan coefficient for a dipole transition. We note that the t-SURFF method is an approximate method for analysis of photoelectrons when applied to this problem with a long-range potential from the remaining ion [40]. Single or multiphoton transitions that populate Rydberg states can also be expected to cause some problems in special cases due to their large radial extent,  $\sim n^2$ .

The angular distribution of the photoelectron can be described by a coherent superposition of partial waves with the corresponding angular momentum given by the dipole selection rules. To find these partial wave amplitudes from the scattering amplitudes,

$b_{\mathbf{k},a}(T)$ , we solve a minimization problem,

$$\tilde{a} = \arg \min_a \sum_i \left| f_q(\theta_i) - \sum_m \left| \sum_\ell a_{\ell m} Y_{\ell m}(\theta_i, \varphi) \right|^2 \right|^2, \quad (10)$$

for the complex amplitudes  $\tilde{a} = \{\tilde{a}_{\ell m}\}$ . The magnetic quantum number of the photoelectron is linked to that of the hole,  $m_p = m_a$ , which is typically unresolved in experiments and, therefore, should be summed over incoherently. In Eq. (10) the angular probability distribution of a peak  $q$  is computed by integrating over energy, that is

$$f_q(\theta_i) = \frac{1}{2} \int_{E_q - \xi}^{E_q + \xi} dE |b_{\mathbf{k}_i, a}(T)|^2, \quad (11)$$

where  $E_q$  is the energy at the center of the peak  $q$ , using Eq. (8) for a given final momentum of the photoelectron,  $k = |\mathbf{k}|$  evaluated at a set of polar angles

$\theta_i$ .

### D. Numerical implementation

Our method is similar to that of Karamatskou et al. [29], as it combines TDCIS for closed-shell atoms [38] with the Time-Dependent Surface Flux (t-SURFF) method [40], but our method differs in a number of ways: (i) our numerical implementation is based on B-splines [41], (ii) we use Exterior Complex Scaling (ECS) to handle the boundary conditions of the outgoing photoelectrons [42], (iii) our implementation of t-SURFF, Eq. (9), differs in its detailed derivation, as discussed in Appendix A.

In this work we restrict the active space configuration in energy,  $E_a^p = \varepsilon_p - \varepsilon_a < 30$  a.u. = 816.33 eV, and use an electron angular momentum of at least  $\ell = 6$ . We also restrict the TDCIS calculation to the outermost valence orbital in the sum over occ in Eq. (2) and, therefore, do not consider XUV-stimulated hole-hole transitions that can lead to further excitation of the ion within TDCIS [43]. The latter restriction implies that we consider the  $1s$  orbital in helium, but only excitation from the  $2p$  orbital in neon. The binding energies used are the Hartree-Fock binding energies  $I_p = 0.918$  a.u. for helium and  $I_p = 0.850$  a.u. for the  $2p$  orbital in neon.

For the B-spline interpolation, we use 165 and 320 knotpoints in the inner region for helium and neon respectively and 30 knotpoints in the ECS region both atoms. The polynomials used are chosen to be of order 6. We use a node spacing of 0.4 a.u. and an ECS-angle of 25 degrees. The use of ECS leads to a non-Hermitian Hamiltonian, where the virtual states are exponentially damped in time by complex eigenvalues. In space the electron wavefunctions remain physical within the radius  $r_{\text{ecs}} = 64$  a.u. for helium and  $r_{\text{ecs}} = 120$  a.u. for neon. Inside the ECS region,  $r > r_{\text{ecs}}$ , the photoelectron wavefunction is damped radially, which helps to remove nonphysical reflections from the end point of the radial knotpoint sequence. The use of ECS restricts the propagation of TDCIS to the velocity gauge.

## III. RESULTS

In this section we present our results from laser-assisted photoionization simulations. We present the numerically obtained angle-resolved photoelectron spectrum alongside the photoelectron angular distribution (PAD) for helium in part A and for neon in part B. We also vary the frequency of the XUV-photon,  $\omega_{\text{XUV}}$ , is varied in order to study how the PAD depends on different final kinetic energies of the photoelectron.

In Fig. 1, the laser-assisted photoionization paths are shown for helium and neon respectively. We denote the peaks in the photoelectron angular distribution, corresponding to local maxima, as in Fig. 1.

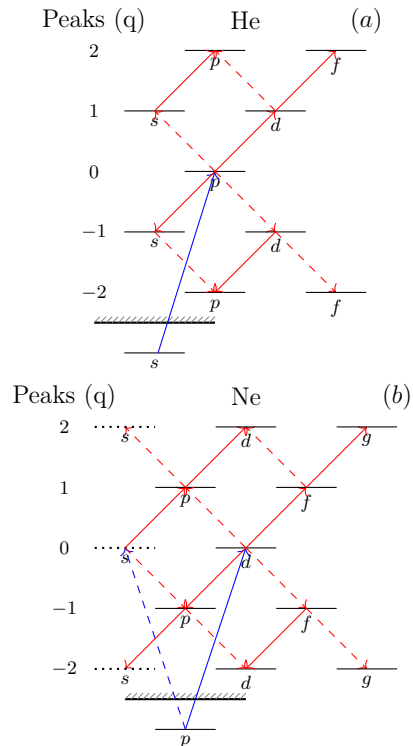


Figure 1. Laser-assisted photoionization paths in (a) helium and (b) neon in the case of absorption or emission of IR-photons. In neon, the dotted  $s$ -states indicate that they are only reachable for the case of  $m = 0$ . The propensity rule is illustrated with filled lines as these transitions are relatively more probable than the transitions of dashed lines when comparing absorption and emission.

For instance, in the  $+1$  and  $-1$  peaks in helium, corresponding to the absorption or emission of one IR-photon, the angular probability distribution results from a superposition of  $\ell = 0$  and  $\ell = 2$ . The photoelectron alters its orbital angular momentum by plus or minus one for each interaction event with the dressing IR-field. The angle-resolved photoelectron spectrum consists of well defined peaks and The the PAD follows the shape of a superposition of spherical harmonics as indicated on the vertical energy scale in Fig 1 due to the fact that the pulse duration is larger than the IR period,  $\tau > 2\pi/\omega_{\text{IR}}$ .

### A. Helium

The obtained angle-resolved photoelectron spectrum in helium is shown in Fig. 2(a) on a logarithmic scale. The main central line corresponds to absorption of one XUV-photon and the sidebands correspond to absorption or emission of  $q$  IR-photons. Alongside the spectrum, the PAD retrieved by Eq. (11) of the absorption and emission sideband peaks are shown in Fig. 2(b) for the first absorption and emission peaks,  $q = \pm 1$ , and Fig. 2(c) for the second absorption and emission peaks,  $q = \pm 2$ . The main line peak,  $q = 0$ ,

is included for reference and the PAD are normalized in the sense that their largest value equals to one in order to be able to compare the shapes with the main line. In the figure, the fitted spherical harmonics using Eq. (10) are also marked on top of the PAD. The PAD shows an asymmetry between absorption and emission of IR-photons in the continuum which is expressed by the different number of minima in the sideband peaks. For example, in the first absorption and emission peaks,  $q = 1$  and  $q = -1$ , we observe two minima and one minimum respectively.

In Fig. 3, we present how the angular distribution depends on the XUV-photon energy for normalized first and second absorption peaks in helium. A uniform filter is applied to smoothen spurious oscillations. Each figure corresponds to multiple laser-assisted photoionization simulations with all parameters fixed except the frequency of the ionizing XUV-field. Higher up in the continuum the multiple minima of the absorption peaks tend towards the center, corresponding to an emission angle of 90 degrees. For both  $q = 1$  and  $q = 2$  the spread of the minima hence decreases and approaches asymptotically the location of the single minimum of the emission peaks  $q = -1$  and  $q = -2$  as the kinetic energy of the photoelectron increases.

## B. Neon

In Fig. 4, the obtained angle-resolved photoionization spectrum in neon is shown alongside normalized PAD of the first and second absorption and emission peaks. Again, the main line is included as reference. The fitted spherical harmonics match well with the angular distribution of the peaks of the sidebands. Contrary to helium, we now have two possible intermediate cases after absorption of an XUV-photon with  $\ell = 0$  and  $\ell = 2$ . In neon we do not observe any qualitative difference in the PAD, comparing the first absorption and emission peaks,  $q = \pm 1$ . Both  $q = 1$  and  $q = -1$  show one single minimum with similar angular shape. However, in the second absorption and emission peaks,  $q = \pm 2$ , there is a clear difference with  $q = 2$  showing two distinct minima and  $q = -2$  showing a single minimum.

To complement our neon studies we also consider the isolated  $m$ -channels. Since we deal with systems of spherical symmetry, the positive  $m = +1$  channel and the negative  $m = -1$  channel will yield the same photoelectron angular distribution, and without loss of generality we can consider it one effective channel. We denote this channel as the *gerade*  $m = \pm 1$  channel. The multiple  $m$  channels in neon is contrary to helium, where we only have one magnetic quantum number,  $m = 0$ . In Fig. 5, the  $m$  angle-resolved photoelectron spectra are presented in neon on a logarithmic scale for  $m = 0$  and  $m = \pm 1$ , respectively, alongside the normalized PAD of the absorption and emission peaks. For the  $m = 0$  channel isolated, the angular distributions of  $q = \pm 1$  show just a slight difference with three shallow minima in absorption and

one in emission. In the  $m = \pm 1$  channel on the other hand, the difference between absorption and emission is more distinct. Here, the angular distribution of  $q = \pm 1$  show four and three minima respectively, including the minima at 0 and 180 degrees. In  $q = \pm 2$ , the difference is clear in both  $m = 0$  and  $m = \pm 1$  channels. In  $m = 0$  we identify two peaks in the case of absorption,  $q = 2$ , and a flat bottom in the case of emission,  $q = -2$ . Although the lack of a clear minimum in  $q = -2$ , the qualitative difference in the shape of the angular distribution is clear. Likewise, in  $m = \pm 1$ , we identify a difference between absorption or emission of two IR-photons,  $q = 2$  and  $q = -2$ . In  $q = 2$  we observe five minima compared to three minima in  $q = -2$ , including the two minima at an emission angle of 0 and 180 degrees.

In Fig. 6, we present the normalized PAD of peaks  $q = 1$  and  $q = 2$  as a function of the XUV-photon energy for neon in the non-resolved  $m$  case, and the two  $m = 0$  and  $m = \pm 1$  channel cases. Again, each figure corresponds to multiple simulations, changing only the frequency of the ionizing XUV-photon. With increasing frequency of the XUV, and hence kinetic energy of the photoelectrons, the minima become more accentuated and localized in the center at an emission angle of 90 degrees for all cases.

## IV. DISCUSSION

The difference of the  $q = 1$  and  $q = -1$  peaks in helium and neon with  $m = \pm 1$  can be described by the extension of Fano's propensity rule, as given by Busto et al. [35], which stipulates that absorption is to a higher degree linked to an increase of angular momentum than emission. At this point it should be noted that in helium, it is not *more* probable to increase the orbital angular momentum after absorbing one IR-photon, since the ratio at the first absorption peak is smaller than unity, but *more* should be viewed in a relative sense compared to emission of one IR-photon. The peaks  $q = \pm 1$  in helium and neon with  $m = \pm 1$  are special cases in which we know completely the angular distribution after the absorption of one XUV-photon. We can thus compare absorption and emission of one IR-photon directly in terms of a propensity rule. However, when we compare the  $q = \pm 2$  peaks in helium and neon with  $m = \pm 1$ , we cannot rely entirely on the effect of the propensity rule to describe the angular distribution. Instead, we also need to take into consideration the two interfering paths leading to the final angular momentum, hereafter coined a *diamond* due to its diagrammatically convincing shape.

The resulting angular distribution is mainly described by these two features. To understand the interplay between the propensity rule and the interference effects of the diamond, we present the ratio of the complex amplitudes  $\tilde{a}_{\ell>}^{\pm q}$ , corresponding to the higher attainable angular momentum, and  $\tilde{a}_{\ell<}^{\pm q}$ , correspond-

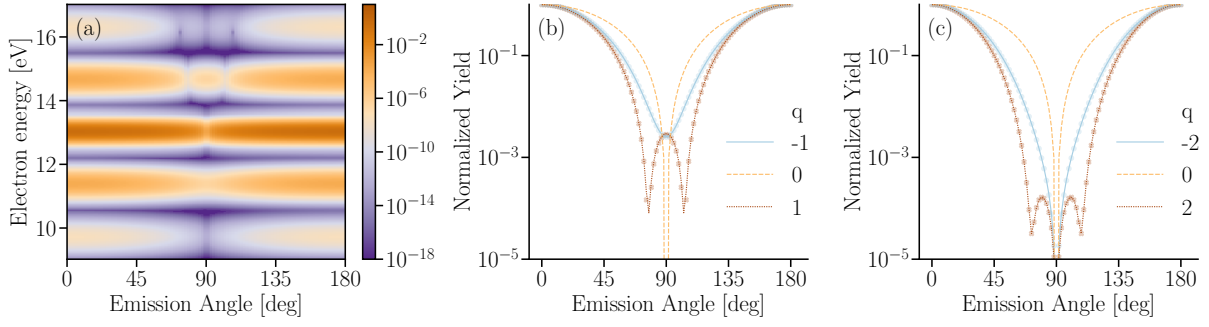


Figure 2. (a) Angle-resolved photoelectron spectrum in helium using an XUV-photon energy of 38 eV. (b) PAD using  $q = \pm 1$  and (c) PAD using  $q = \pm 2$ . The dots are retrieved by minimizing the squared-distance to expected spherical harmonics.

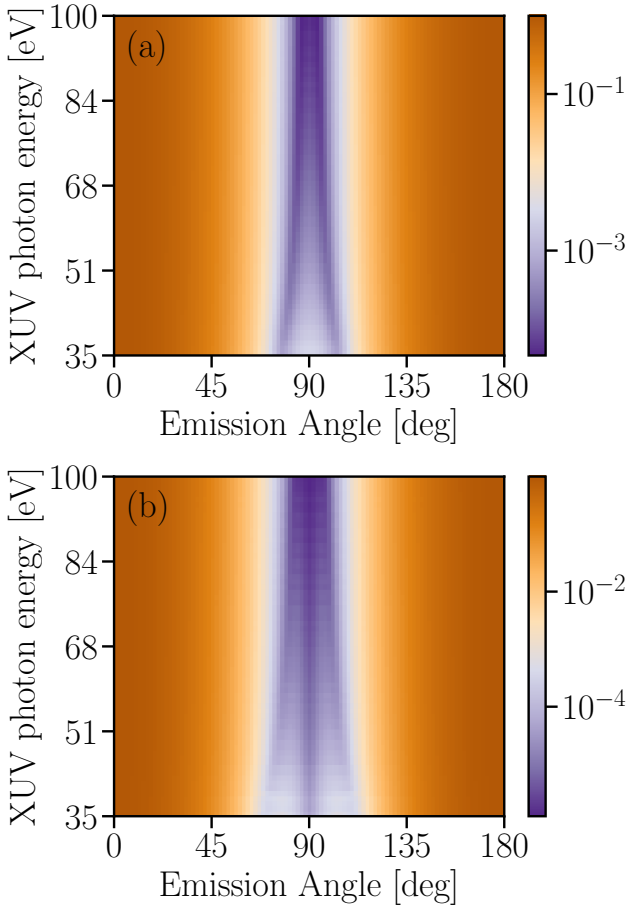


Figure 3. PAD of helium peaks (a)  $q = 1$  and (b)  $q = 2$  as a function of XUV-photon energy.

ing to the lower, for varying XUV-photon energy in helium and neon with  $m = \pm 1$  in Fig. 7. In the high-energy limit of the photoelectron, the ratio approaches asymptotically a value determined by the angular part of the dipole matrix element included in Fig. 7 as a gray dotted line. The angular dipole matrix element ratio of the upper and lower attained angular momen-

tum in helium is given by

$$\left| \frac{\tilde{a}_{\ell>}^{\pm 1}}{\tilde{a}_{\ell<}^{\pm 1}} \right| \rightarrow \left| \frac{\langle Y_{20}|Y_{10}|Y_{10} \rangle}{\langle Y_{00}|Y_{10}|Y_{10} \rangle} \right| = \frac{2}{\sqrt{5}}, \quad (12)$$

and

$$\left| \frac{\tilde{a}_{\ell>}^{\pm 2}}{\tilde{a}_{\ell<}^{\pm 2}} \right| \rightarrow \left| \frac{\langle Y_{30}|Y_{10}|Y_{20} \rangle \langle Y_{20}|Y_{10}|Y_{10} \rangle}{|\langle Y_{10}|Y_{10}|Y_{20} \rangle|^2 + |\langle Y_{10}|Y_{10}|Y_{00} \rangle|^2} \right| = \frac{2}{\sqrt{21}}, \quad (13)$$

for the  $q = \pm 1$  and  $q = \pm 2$  peaks respectively. In neon,  $m = \pm 1$ , the ratios are

$$\left| \frac{\tilde{a}_{\ell>}^{\pm 1}}{\tilde{a}_{\ell<}^{\pm 1}} \right| \rightarrow \left| \frac{\langle Y_{31}|Y_{11}|Y_{21} \rangle}{\langle Y_{11}|Y_{11}|Y_{21} \rangle} \right| = \sqrt{\frac{8}{7}}, \quad (14)$$

for the  $q = \pm 1$  peaks and

$$\left| \frac{\tilde{a}_{\ell>}^{\pm 2}}{\tilde{a}_{\ell<}^{\pm 2}} \right| \rightarrow \left| \frac{\langle Y_{41}|Y_{11}|Y_{31} \rangle \langle Y_{31}|Y_{11}|Y_{21} \rangle}{|\langle Y_{21}|Y_{11}|Y_{31} \rangle|^2 + |\langle Y_{21}|Y_{11}|Y_{11} \rangle|^2} \right| = \frac{\sqrt{8}}{3\sqrt{3}}, \quad (15)$$

for the  $q = \pm 2$  peaks. For the  $q = \pm 1$  peaks, Eq. (12) and Eq. (14), the values are *close to one*, and for the  $q = \pm 2$  peaks, Eq. (13) and Eq. (15), the asymptotic values are *close to one half* since the dipole matrix elements from some  $\ell$  to  $\ell \pm 1$  all have comparable magnitude to the dipole matrix elements which links another  $\ell'$  to  $\ell' \pm 1$ , for  $\ell \approx \ell'$ . In fact, the smaller the relative difference of  $\ell$  and  $\ell'$ , the more comparable the magnitudes of the dipole matrix elements are. This explains why the asymptotic value reached at  $q = \pm 2$  in neon,  $m = \pm 1$ , is closer to one half than the asymptotic value reach at  $q = \pm 2$  in helium. Although the matrix elements in the denominator for peaks with  $q = \pm 2$  are taken absolute-squared, one should not be tempted to view the effect of the diamond incoherently. In principle, there could be any phase difference between the two terms but the fact that there is a plus-sign between the two terms requires that the superposition is not only coherent but also that there is no phase difference between the two paths to the final angular momentum state. This fact that there is not a negative phase difference between different angular momentum paths can be explained

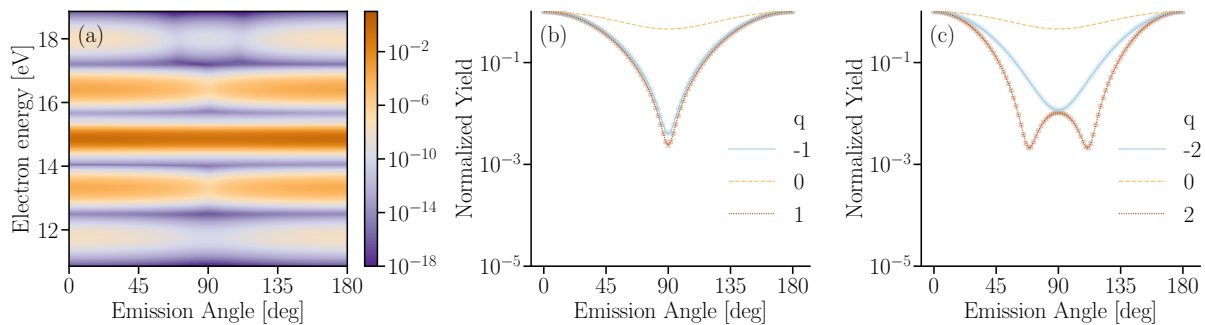


Figure 4. (a) Angle-resolved photoelectron spectrum in neon  $2p$  using an XUV-photon energy of 38 eV. (b) PAD using  $q = \pm 1$  and (c) PAD using  $q = \pm 2$ . The dots are retrieved by minimizing the squared-distance to expected spherical harmonics.

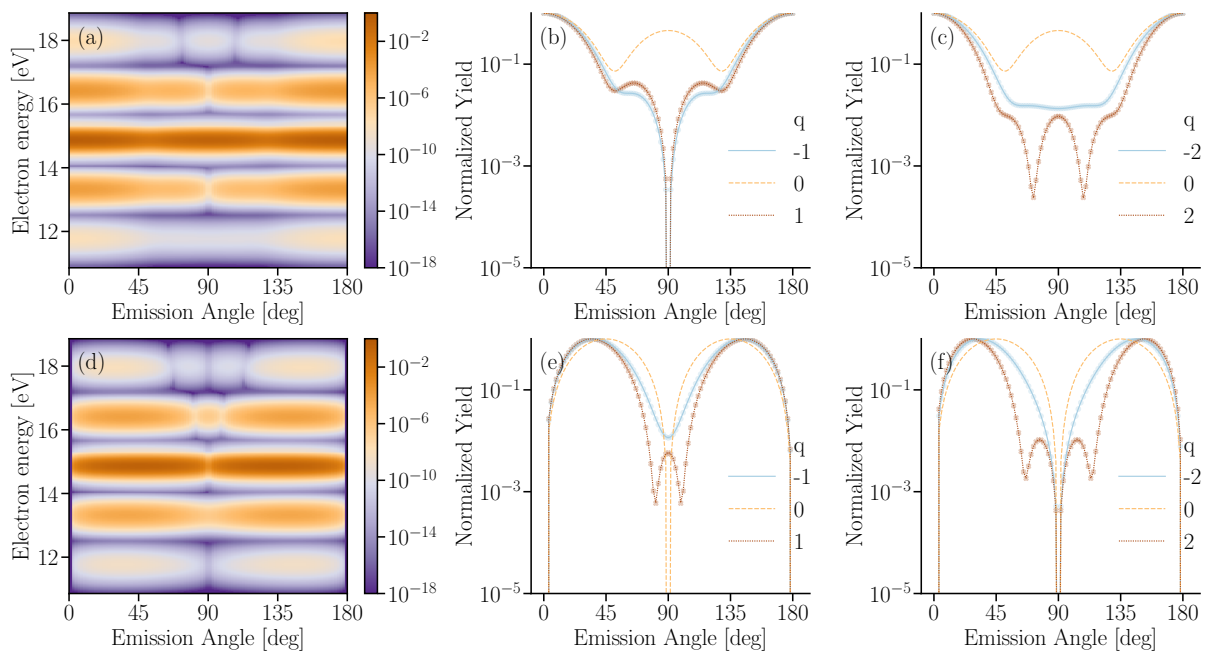


Figure 5. Angle-resolved photoelectron spectrum in neon  $2p$  with (a)  $m = 0$  and (d)  $m = \pm 1$ , using an XUV-photon energy of 38 eV. (b) and (e) PAD using  $q = \pm 1$  and (c) and (f) PAD using  $q = \pm 2$ . The dots are retrieved by minimizing the squared-distance to expected spherical harmonics.

by the continuum–continuum phase that they acquire in the laser-stimulated transitions [44].

We argue that in the high-energy limit, the main feature is explained by the diamond and the propensity rule is in the margin. However, the propensity rule alone explains why there is a difference between the angular probability distributions in absorption and emission and is, although small compared to the effect of the diamond, important to explain the appearance of minima in the angular distribution. In fact, close to the ionization barrier, the propensity rule is the main component to describe the angular probability distributions of absorption and emission and not only the difference between them. The  $q = 2$  peak in neon  $m = \pm 1$  is a good example of the importance of this interplay. In the  $q = 2$  peak in neon  $m = \pm 1$ , the paths of increasing–decreasing or decreasing–increasing angular momen-

tum,  $\ell = 1 \rightarrow \ell = 0 \rightarrow \ell = 1$  and  $\ell = 1 \rightarrow \ell = 2 \rightarrow \ell = 1$ , are individually weaker than the path of two times increasing the orbital angular momentum,  $\ell = 1 \rightarrow \ell = 2 \rightarrow \ell = 3$ , but the constructive interference impacts the relative amount of angular momentum content heavily to favour a decrease in the high-energy limit. Contrary, for low kinetic energy of the photoelectron, absorption and emission

Finally, the absence of a difference between absorption and emission in the  $q = 1$  peak of neon, without resolution in  $m$ , in our calculations does not impose any restrictions to measure a time-delay in the photoionization but indicates that the origin of it is more deeply intertwined in the non-resolved  $m$  channel and that the angular dependency is hidden in the two effective  $m$  channels. Ivanov and Kheifets observed that the atomic delay in neon depends strongly on the  $m = 0$  channel [45], which was related to the

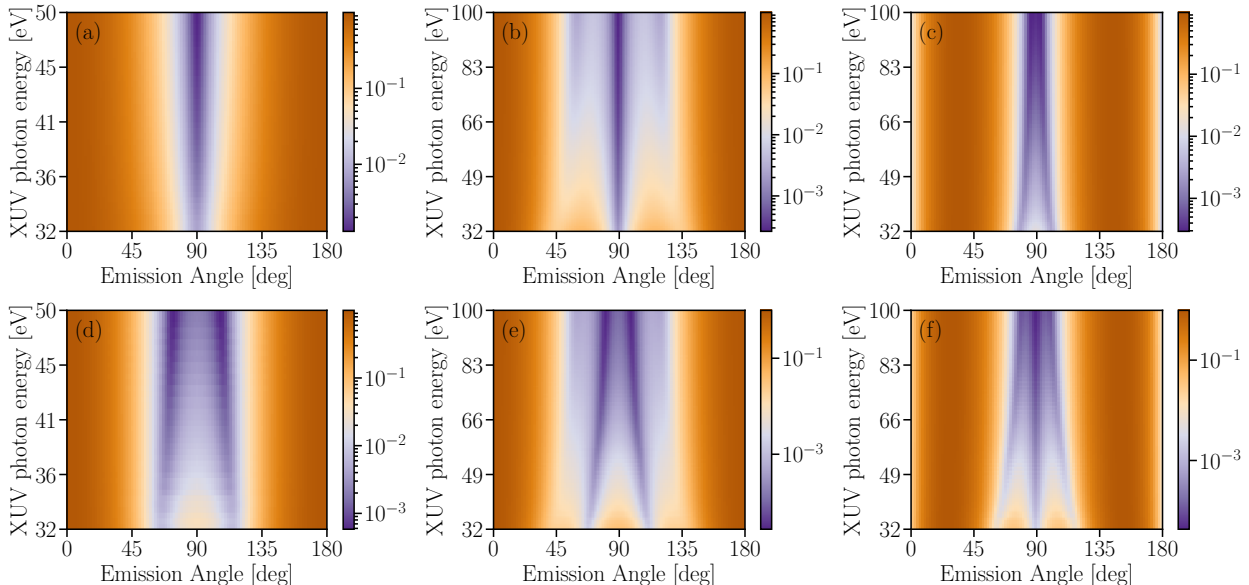


Figure 6. PAD of neon as a function of XUV-photon energy for peaks (a)  $q = 1$  unresolved in  $m$ , (b)  $q = 1$  with  $m = 0$ , (c)  $q = 1$  with  $m = \pm 1$ , (d)  $q = 2$  unresolved in  $m$ , (e)  $q = 2$  with  $m = 0$  and (f)  $q = 2$  with  $m = \pm 1$ .

occurrence of a  $\pi$ -shift in the absorption path but not in the emission path and why this leads to strong angle-dependent delays by Busto et al. [35]. By resolving the  $m$  channels, the effect of the propensity rules is clear already at the first absorption and emission peaks. This motivates experiments with resolution of the magnetic quantum number when studying the photoionization time-delay in order to reveal hidden angular dependency.

## V. CONCLUSIONS

With the TDCIS and t-SURFF approach, we are able to retrieve the photoelectron angular distribution in order to study the difference between absorption and emission of photons in the continuum. We confirm the generalization of Fano's propensity rule by extending it to include continuum-continuum absorption and emission processes and that this propensity effect is of less importance higher up in the continuum where the centrifugal potential is small compared to the kinetic energy of the photoelectron, in accordance with Busto et al. [35]. We repeat the predictions in helium for the angular dependency of the probability distribution in the event of absorption and emission of one IR-photon in the continuum, and further move forward to study the absorption and emission of two IR-photons. Further, we find that the effect of the propensity rule is accumulated, but that multiple interfering paths leading to the same angular momentum state is a stronger process for photoelectrons with high kinetic energy, which always favour a decrease in the angular momentum. While the interference effects impact the most on the angular distribution for photoelectrons with a sufficiently high kinetic energy, it is

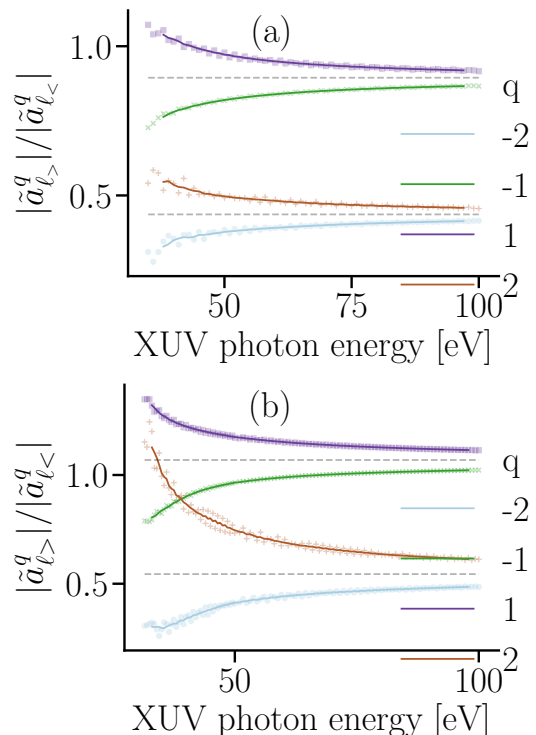


Figure 7. Ratio of the magnitude of the coefficients of fitted spherical harmonics of the peaks of the angle-resolved photoelectron angular distribution as a function of XUV-photon energy in (a) helium and (b) neon,  $m = \pm 1$ .

the propensity rules that lead to a difference between absorption and emission.



## Appendix A: Comparison of the final expression

Compared to the expression given in Eq. (22) by Karamatskou et al. [29], we do not obtain the same analytical expression. On the second line of Eq. (9), we have a factor

$$(kr_c j_{\ell_p}(kr_c) + j_{\ell_p}(kr_c))$$

whereas they have (given in our notation)

$$\left(-j_{\ell_p}(kr_c) + \frac{kr_c}{2} j'_{\ell_p}(kr_c) - \frac{1}{2} j_{\ell_p}(kr_c)\right),$$

and on the third line, we have an  $r_c$  which is not present in their work. We speculate that our faster convergence in time may be due to this discrepancy in the analytical expressions.

- 
- [1] Anthony F. Starace. Theory of Atomic Photoionization. *Handbuch der Physik*, 6, 1982.
- [2] M. Ya. Amusia. *Atomic photoeffect*. Plenum Press, New York, 1990.
- [3] A. S. Kheifets. Time delay in valence-shell photoionization of noble-gas atoms. *Phys. Rev. A*, 87:063404, 2013.
- [4] U. Fano. Propensity rules: An analytical approach. *Phys. Rev. A*, 32(1):617–618, July 1985.
- [5] John W. Cooper. Photoionization from outer atomic subshells. a model study. *Phys. Rev.*, 128:681–693, Oct 1962.
- [6] E A Seddon, J A Clarke, D J Dunning, C Masciovecchio, C J Milne, F Parmigiani, D Rugg, J C H Spence, N R Thompson, K Ueda, S M Vinko, J S Wark, and W Wurth. Short-wavelength free-electron laser sources and science: a review. *Reports on Progress in Physics*, 80(11):115901, oct 2017.
- [7] E. Allaria, F. Bencivenga, R. Borghes, F. Capotondi, D. Castronovo, P. Charalambous, P. Cinquegrana, M. B. Danailov, G. De Ninno, A. Demidovich, S. Di Mitri, B. Diviacco, D. Fausti, W. M. Fawley, E. Ferrari, L. Froehlich, D. Gauthier, A. Gessini, L. Giannessi, R. Ivanov, M. Kiskinova, G. Kurdi, B. Mahieu, N. Mahne, I. Nikolov, C. Masciovecchio, E. Pedersoli, G. Penco, L. Raimondi, C. Serpico, P. Sigalotti, S. Spampinati, C. Spezzani, C. Svetina, M. Trovò, and M. Zangrando. Two-colour pump-probe experiments with a twin-pulse-seed extreme ultraviolet free-electron laser. *Nature Communications*, 4(1):2476, 2013.
- [8] A. A. Lutman, R. Coffee, Y. Ding, Z. Huang, J. Krzywinski, T. Maxwell, M. Messerschmidt, and H.-D. Nuhn. Experimental demonstration of femtosecond two-color x-ray free-electron lasers. *Phys. Rev. Lett.*, 110:134801, Mar 2013.
- [9] David Gauthier, Primož Rebernik Ribič, Giovanni De Ninno, Enrico Allaria, Paolo Cinquegrana, Miltcho Bojanov Danailov, Alexander Demidovich, Eugenio Ferrari, and Luca Giannessi. Generation of phase-locked pulses from a seeded free-electron laser. *Phys. Rev. Lett.*, 116:024801, Jan 2016.
- [10] Ferenc Krausz and Misha Ivanov. Attosecond physics. *Rev. Mod. Phys.*, 81:163–234, 2009.
- [11] S. Düsterer, L. Rading, P. Johnsson, A. Rouzée, A. Hundertmark, M. J. J. Vrakking, P. Radcliffe, M. Meyer, A. K. Kazansky, and N. M. Kabachnik. Interference in the angular distribution of photoelectrons in superimposed XUV and optical laser fields. *J. Phys. B: At. Mol. Opt. Phys.*, 46(16):164026, August 2013.
- [12] S. Düsterer, G. Hartmann, C. Bomme, R. Boll, J. T. Costello, B. Erk, A. De Fanis, M. Ilchen, P. Johnsson, T. J. Kelly, B. Manschwetus, T. Mazza, M. Meyer, C. Passow, D. Rompotis, L. Varvarezos, A. K. Kazansky, and N. M. Kabachnik. Two-color XUV+NIR femtosecond photoionization of neon in the near-threshold region. *New J. Phys.*, 21(6):063034, June 2019.
- [13] Norman M. Kroll and Kenneth M. Watson. Charged-Particle Scattering in the Presence of a Strong Electromagnetic Wave. *Phys. Rev. A*, 8:804–809, August 1973.
- [14] Lars Bojer Madsen. Strong-field approximation in laser-assisted dynamics. *American Journal of Physics*, 73(1):57–62, 2005.
- [15] Álvaro Jiménez Galán, Luca Argenti, and Fernando Martín. The soft-photon approximation in infrared-laser-assisted atomic ionization by extreme-ultraviolet attosecond-pulse trains. *New Journal of Physics*, 15(11):113009, 2013.
- [16] E S Toma and H G Muller. Calculation of matrix elements for mixed extreme-ultraviolet–infrared two-photon above-threshold ionization of argon. *Journal of Physics B: Atomic, Molecular and Optical Physics*, 35(16):3435, 2002.
- [17] J.M. Dahlström, D. Guénot, K. Klünder, M. Gisselbrecht, J. Mauritsson, A. L’Huillier, A. Maquet, and R. Taïeb. Theory of attosecond delays in laser-assisted photoionization. *Chemical Physics*, 414(0):53 – 64, 2013.
- [18] J. M. Dahlström, T. Carette, and E. Lindroth. Diagrammatic approach to attosecond delays in photoionization. *Phys. Rev. A*, 86:061402, 2012.
- [19] Eva Lindroth and Jan Marcus Dahlström. Attosecond delays in laser-assisted photodetachment from closed-shell negative ions. *Phys. Rev. A*, 96:013420, Jul 2017.
- [20] Jimmy Vinbladh, Jan Marcus Dahlström, and Eva Lindroth. Many-body calculations of two-photon, two-color matrix elements for attosecond delays. *Phys. Rev. A*, 100:043424, Oct 2019.
- [21] C.-H. Zhang and U. Thumm. Electron-ion interaction effects in attosecond time-resolved photoelectron spectra. *Phys. Rev. A*, 82:043405, 2010.
- [22] S Nagele, R Pazourek, J Feist, K Doblhoff-Dier, C Lemell, K Tőkési, and J Burgdörfer. Time-resolved photoemission by attosecond streaking: extraction of time information. *Journal of Physics B: Atomic, Molecular and Optical Physics*, 44:081001, 2011.
- [23] I. A. Ivanov and A. S. Kheifets. Angle-dependent time delay in two-color xuv+ir photoemission of he and ne. *Phys. Rev. A*, 96:013408, Jul 2017.
- [24] Alexander W. Bray, Faiza Naseem, and Anatoli S. Kheifets. Simulation of angular-resolved rabbit measurements in noble-gas atoms. *Phys. Rev. A*, 97:063404, Jun 2018.

- [25] Renate Pazourek, Johannes Feist, Stefan Nagele, and Joachim Burgdörfer. Attosecond streaking of correlated two-electron transitions in helium. *Phys. Rev. Lett.*, 108:163001, 2012.
- [26] L. R. Moore, M. A. Lysaght, J. S. Parker, H. W. van der Hart, and K. T. Taylor. Time delay between photoemission from the  $2p$  and  $2s$  subshells of neon. *Phys. Rev. A*, 84:061404, 2011.
- [27] M. A. Lysaght, H. W. van der Hart, and P. G. Burke. Time-dependent  $S$ -matrix theory for ultrafast atomic processes. *Phys. Rev. A*, 79(5):053411, May 2009.
- [28] Shunsuke A. Sato, Hannes Hübener, Angel Rubio, and Umberto De Giovannini. First-principles simulations for attosecond photoelectron spectroscopy based on time-dependent density functional theory. *The European Physical Journal B*, 91(6):126, Jun 2018.
- [29] Antonia Karamatskou, Stefan Pabst, Yi-Jen Chen, and Robin Santra. Calculation of photoelectron spectra within the time-dependent configuration-interaction singles scheme. *Phys. Rev. A*, 89:033415, Mar 2014.
- [30] Yuki Orimo, Takeshi Sato, and Kenichi L. Ishikawa. Application of the time-dependent surface flux method to the time-dependent multiconfiguration self-consistent-field method. *Phys. Rev. A*, 100(1):013419, July 2019.
- [31] P. M. Paul, E. S. Toma, P. Breger, G. Mullot, F. Augé, Ph. Balcou, H. G. Muller, and P. Agostini. Observation of a train of attosecond pulses from high harmonic generation. *Science*, 292(5522):1689–1692, 2001.
- [32] M. Schultze, M. Fiess, N. Karpowicz, J. Gagnon, M. Korbman, M. Hofstetter, S. Neppl, A. L. Cavalieri, Y. Komninos, Th. Mercouris, C. A. Nicolaides, R. Pazourek, S. Nagele, J. Feist, J. Burgdörfer, A. M. Azzeer, R. Ernstorfer, R. Kienberger, U. Kleineberg, E. Goulielmakis, F. Krausz, and V. S. Yakovlev. Delay in photoemission. *Science*, 328:1658–1662, 2010.
- [33] M. Isinger, R. J. Squibb, D. Busto, S. Zhong, A. Harth, D. Kroon, S. Nandi, C. L. Arnold, M. Miranda, J. M. Dahlström, E. Lindroth, R. Feifel, M. Gisselbrecht, and A. L’Huillier. Photoionization in the time and frequency domain. *Science*, 358(6365):893–896, November 2017.
- [34] Sebastian Heuser, Álvaro Jiménez Galán, Claudio Cirelli, Carlos Marante, Mazyar Sabbar, Robert Boge, Matteo Lucchini, Lukas Gallmann, Igor Ivanov, Anatoli S. Kheifets, J. Marcus Dahlström, Eva Lindroth, Luca Argenti, Fernando Martín, and Ursula Keller. Angular dependence of photoemission time delay in helium. *Phys. Rev. A*, 94:063409, Dec 2016.
- [35] D. Busto, J. Vinbladh, S. Zhong, M. Isinger, S. Nandi, S. Maclot, P. Johnsson, M. Gisselbrecht, A. L’Huillier, E. Lindroth, and J. M. Dahlström. Fano’s Propensity Rule in Angle-Resolved Attosecond Pump-Probe Photoionization. *Phys. Rev. Lett.*, 123(13):133201, September 2019.
- [36] Claudio Cirelli, Carlos Marante, Sebastian Heuser, C. L. M. Petersson, Álvaro Jiménez Galán, Luca Argenti, Shiyang Zhong, David Busto, Marcus Isinger, Saikat Nandi, Sylvain Maclot, Linnea Rading, Per Johnsson, Mathieu Gisselbrecht, Matteo Lucchini, Lukas Gallmann, J. Marcus Dahlström, Eva Lindroth, Anne L’Huillier, Fernando Martín, and Ursula Keller. Anisotropic photoemission time delays close to a Fano resonance. *Nat Commun*, 9(1):1–9, March 2018.
- [37] Nina Rohringer, Ariel Gordon, and Robin Santra. Configuration-interaction-based time-dependent orbital approach for *ab initio* treatment of electronic dynamics in a strong optical laser field. *Phys. Rev. A*, 74:043420, 2006.
- [38] Loren Greenman, Phay J. Ho, Stefan Pabst, Eugene Kamarchik, David A. Mazziotti, and Robin Santra. Implementation of the time-dependent configuration-interaction singles method for atomic strong-field processes. *Phys. Rev. A*, 82:023406, 2010.
- [39] Stefan Pabst, Loren Greenman, David A. Mazziotti, and Robin Santra. Impact of multichannel and multipole effects on the cooper minimum in the high-order-harmonic spectrum of argon. *Phys. Rev. A*, 85:023411, Feb 2012.
- [40] Liang Tao and Armin Scrinzi. Photo-electron momentum spectra from minimal volumes: the time-dependent surface flux method. *New Journal of Physics*, 14:013021, 2012.
- [41] Carl deBoor. *A Practical Guide to Splines*. Springer-Verlag, New York, 1978.
- [42] Barry Simon. The definition of molecular resonance curves by the method of exterior complex scaling. *Physics Letters A*, 71(2–3):211 – 214, 1979.
- [43] Jhih-An You, Nina Rohringer, and Jan Marcus Dahlström. Attosecond photoionization dynamics with stimulated core-valence transitions. *Phys. Rev. A*, 93:033413, Mar 2016.
- [44] J M Dahlström, A L’Huillier, and A Maquet. Introduction to attosecond delays in photoionization. *Journal of Physics B: Atomic, Molecular and Optical Physics*, 45:183001, 2012.
- [45] I. A. Ivanov and A. S. Kheifets. Angle-dependent time delay in two-color XUV+IR photoemission of He and Ne. *Phys. Rev. A*, 96(1):013408, July 2017.